

Compressive property and shape memory effect of 3D printed continuous ramie fiber reinforced biocomposite corrugated structures

Ping Cheng^{1,2}, Kui Wang¹, Xuanzhen Chen¹, Antoine Le Duigou³, Yong Peng^{1*}, Wei Wen⁴

¹ Key Laboratory of Traffic Safety on Track of Ministry of Education, School of Traffic & Transportation Engineering, Central South University, Changsha 410075, China

² ICUBE Laboratory-CNRS, University of Strasbourg, Strasbourg 67000, France

³ IRDL UMR CNRS 6027, Bionics group, University of South Brittany, F-56100 Lorient, France

⁴ Department of Engineering, Lancaster University, Lancaster, LA1 4YR, UK

*Corresponding author e-mail address: yong_peng@csu.edu.cn

Abstract

The present work aimed to study the quasi-static compression behaviors of 3D printed continuous ramie fiber reinforced biocomposite corrugated structures (CFCSs) with excellent shape memory effects. The in-plane compression test was conducted to evaluate the effects of cell shapes, fiber volume fraction (f_v) and addition of fiber on the compression behaviors and energy absorption characteristics of the corrugated structures. The results showed that the compression property and energy absorption capacity of the 3D printed CFCSs increased with decreasing f_v and the addition of continuous ramie yarn. The 3D printed continuous ramie fiber reinforced biocomposite with inverted trapezoid cell shape corrugated structures (CFITCSs) outperformed other cell shapes in the compression strength and specific energy

absorption. The analytical model for the in-plane compression strength of CFITCSs was derived, and predictions were in good agreement with measurements. In addition, continuous natural fiber reinforced composite structure for shape memory was proposed for the first time. The shape recovery testing results demonstrated that 3D printed CFCs had the potential to be a key element of lightweight programmable smart systems.

Keywords: 3D printing; continuous ramie fiber; corrugated structure; shape memory.

1. Introduction

Composite lightweight structures attract considerable attention due to their advantages such as high stiffness-to-weight and excellent energy absorption capacity in recent decades [1, 2]. These structures are therefore widely used in rail transit, aerospace, construction, packaging and other fields [3, 4]. The macroscopic performance of the lightweight structures can be tailored by adjusting the raw material, the cell structure, and the manufacturing process [5]. In previous studies, a large number of composite lightweight structures composed of honeycomb-like, truss, and corrugated cells have been manufactured through the traditional processes [6, 7]. However, the traditional manufacturing processes such as hot-pressing molding, injection molding, vacuum-assisted molding, and filament winding have complex manufacturing processes and require a complex rigid mold, which hinders the wide application of composite lightweight structures [8, 9].

Additive manufacturing (AM) offers the opportunity to easily and rapidly fabricate lightweight structures with complex cell shapes [10, 11]. AM techniques for

polymers and polymer-based composite structures include stereolithography (SLA) technique for liquid photopolymer [12], selective laser sintering (SLS) for polymer powders [13], fused filament fabrication (FFF) for polymer filaments, etc. [14]. Among these methods, FFF has become one of the most common techniques to manufacture lightweight structures [15, 16]. Nevertheless, the relatively poor mechanical performance of pure polymer and short fiber reinforced polymer composites structures manufactured by the FFF approach [17, 18]. Thus, continuous fibers are increasingly used as reinforcement in FFF printed lightweight structures to improve their mechanical properties [19, 20]. Furthermore, shape memory polymers (SMPs) have attracted more attention for their application in AM lightweight structures to achieve better geometrically reconfigurability and functionally deployability [21-23].

Currently, continuous fiber reinforced thermoplastic polymer composite lightweight structures have been successfully manufactured through 3D printing process. Tian et al. [24] proposed a novel integrated manufacturing process for 3D printing of continuous carbon fiber reinforced composite lightweight structures, and which has great potential for manufacturing complex-shaped lightweight carbon fiber composite structures. Matsuzaki et al. [25] evaluated the bending performance of continuous carbon fiber reinforced composite sandwich structures with different core shapes fabricated by 3D printing. The results showed that maximum load and flexural modulus increased as effective density increased for all core shapes. Quan et al. [26] evaluated the compressive property of continuous Kevlar® fiber reinforced composite

auxetic honeycomb structures. The results of established finite element simulation could be in good agreement with the experimental measurements. Dong et al. [21, 27] assessed the tensile properties and shape memory performance of Kevlar® continuous fiber reinforced diamond cellular structural composites. It proved that the increase of fiber content led to a higher tensile property of composite structures. Zeng et al. [28, 29] studied the mechanical properties and shape recovery effects of 3D printed continuous carbon fiber reinforced composite honeycomb structures (CFRCHSs) and corrugated sandwich structures (CFRCTCSs) with various cell shapes. It was observed that CFRCHSs and CFRCTCSs owned excellent energy absorption and shape memory capabilities.

In most of the existing studies, scholars focused on 3D printing continuous synthetic fibers reinforced composite structures due to their widespread application in traditional composite manufacturing [30, 31]. Nevertheless, as the global ecological environment faces increasingly severe challenges, composites with synthetic fibers reinforcement cannot meet today's requirements in terms of environmental friendliness and sustainable development [32]. Increasing use of non-biodegradable polymers and synthetic fibers has become a major environmental threat. Consequently, consideration of environmental problems in the development of composite materials is essential [33-35]. Under these circumstances, the manufacturing of continuous vegetal fiber filled biodegradable polymer composite lightweight structures via 3D printing should receive more attention [5].

The present work focused on the compression property and shape memory effect

of the continuous ramie fiber reinforced biocomposite corrugated structures (CFCSs) fabricated by in-situ impregnation 3D printing process. The compression test was performed to obtain the mechanical response and energy absorption capacity of the CFCSs. The relationships between cell shape, fiber volume fraction (f_v), and continuous fiber reinforcement and compression behaviors were revealed. Finally, the shape recovery tests were performed to evaluate the potential for developing 3D printed smart biocomposite structures.

2. Experimental method

2.1 Design of corrugated structures and printing path

The corrugated structure was usually used to evaluate the structural performance of 3D printed continuous fiber reinforced composites [24]. The shapes of the cell affected the mechanical properties of these corrugated structures. In this study, three corrugated structures with different cell shapes were designed and fabricated, as shown in Fig. 1. The three corrugated structures, composed of the trapezoid, inverted trapezoid and rectangular cells (Fig. 1 (a)), were all 60 mm in length (L), 17 mm in width (W), 20 mm in thickness (H) and 15 mm in cell dimensions (d) [24, 28, 36] (Fig. 1 (b)). The printing paths for the odd and even layers were different because the printing was supposed to be completed without nozzle jumping. These printing schemes are shown in Fig. 1 (c). The printing of a single layer was completed in the x-y plane, and the printing path began from the “S” (start point) and ended at the “E” (end point) according to the direction of the arrows. In this study, samples filled with four different fiber volume fraction (f_v) were chosen for each corrugated structure

(24.3%, 26.8%, 33.9%, 39.1%). The cell wall thicknesses corresponding to the four fiber volume fractions from low to high were 2.3, 2.1, 1.7 and 1.5 mm, respectively. Here, the linear density of the yarn was 36 Nm/2R, and the f_v of the sample was changed by controlling the amount of matrix. In addition to samples with four fiber contents, the corresponding fiber-free matrix samples were manufactured for comparison.

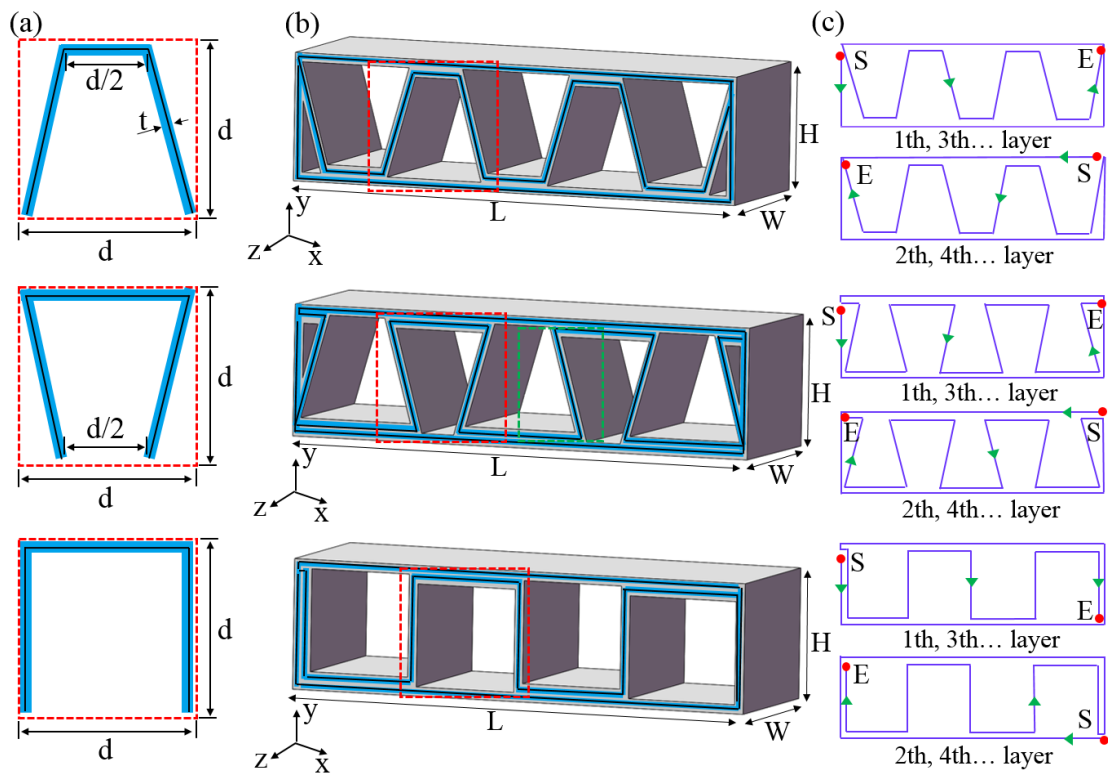


Fig. 1. The geometric configurations of the proposed (a) various cell shapes, (b) corrugated structures and (c) printing paths.

2.2 Materials and processing

In this study, continuous ramie yarns were chosen as reinforcement phase due to their suitable mechanical properties. The ramie yarns were twisted (400 turns/meter) with a linear density of 36 Nm/2R (Dongting Ramie Textile Co. in China). As shown

in Fig. 2, ramie yarn had an average diameter of 350 μm , and ramie fibers had a diameter between 20 and 40 μm . [37]. The ramie yarns were first dried at 80°C for two hours before printing [38]. Commercial polylactic acid (PLA) filaments with a diameter of 1.75 mm were purchased from eSUN Industrial Co., Ltd., China.

A 3D printing equipment (Combot-200, Fibertech, Shanxi, China) based on the FFF technique was used to manufacture the corrugated structures. Ramie yarns and PLA filament were simultaneously fed into the nozzle during printing, whereby the matrix impregnated the yarns in situ. The printing parameters and conditions were set to a layer thickness of 0.3 mm, a printing speed of 100 mm/min, a nozzle temperature of 210 °C, and a bed temperature of 50 °C [39].

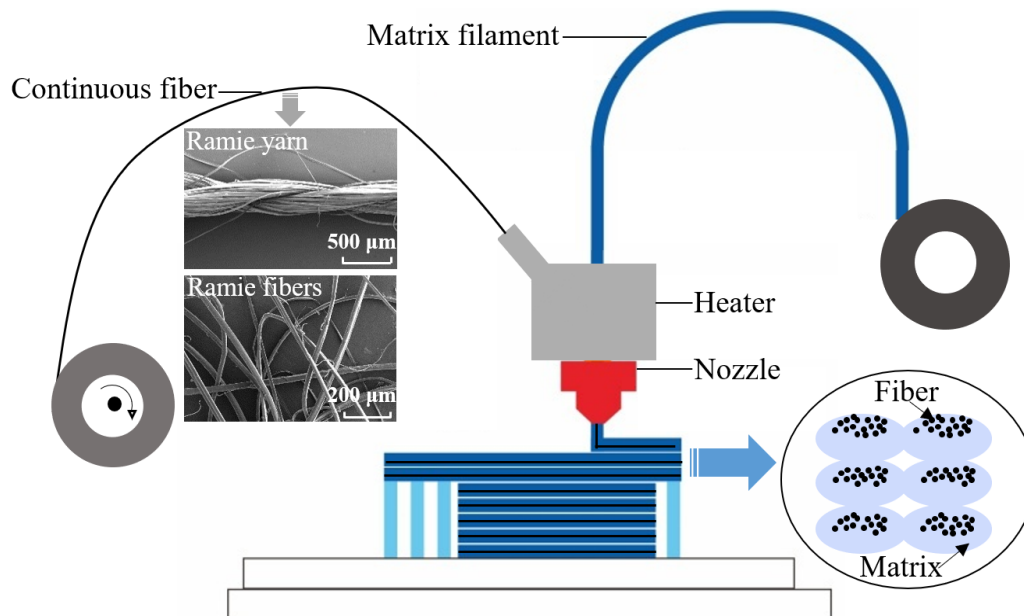


Fig. 2. Method for manufacturing the biocomposite by the FFF.

2.3 Testing and characterization

The quasi-static in-plane compression tests were carried out to investigate the deformation patterns, initial peak force (IPF) and specific energy absorption (SEA) of

the 3D printed corrugated structures. The compressive tests of the samples were performed using a universal mechanical testing machine (E44, MTS Co., USA) at room temperature, and the loading mode was displacement control with a loading rate of 2 mm/min according to ASTM D1621. The samples were compressed to the densification stage at a same compression displacement. Based on the experimentally measured load-displacement curves, energy absorption (EA) could be calculated by using Eq. (1).

$$EA = \int_0^{\delta_d} F d\delta \quad (1)$$

where, δ_d represents the maximum compression displacement at the onset of the densification stage and F denotes the compression load. SEA was the ratio of EA to the mass m of the sample, as shown below

$$SEA = \frac{EA}{m} \quad (2)$$

The initial peak force (IPF) was defined as the first maximum load during the compression process.

The PLA material could recover its original shape after being fixed into a temporary shape by mechanical deformation through a cold/heat programming approach. In this work, the cold programming technique was used to program the CFCSs composed of inverted trapezoid cell at room temperature, which was below their glassy transition temperature (T_g). For the shape programming and recovery process, (1) compression :the sample was first plastically deformed beyond its yield point at a temperature lower than its T_g, (2) unloading: samples were unloaded and kept to a temporary deformed shape, (3) recovery: after programming, the sample

was heated up above its T_g to recover its initial shape, (4) cooling: the shape-recovered samples were naturally cooled at room temperature. The recovery time and process of the structure were recorded simultaneously. Here, the printed structures with different f_v were loaded to the same compression displacement, and the thickness of the compressed sample was 4.7mm (sample was compressed to the densification stage). In addition, the differential scanning calorimeter (DSC, Mettler Toledo, Switzerland) was used to evaluate the thermal behavior of the PLA matrix. PLA filament and PLA sample were heated from room temperature to 230 °C under a nitrogen atmosphere at a rate of 10 °C/min.

The in-plane compression and shape recovery processes were recorded by the high-resolution digital camera (EOS 5D, Mark IV, Canon, Japan) with the combination of a macro lens (EF 100 mm, Canon, Japan). The local morphology of the CFCSs after compression failure was characterized by Field Emission Scanning Electron Microscopy (Hitachi Co., S-4800, Japan). A minimum of three tests were performed for each sample type to ensure reproducibility.

3. Result and discussion

3.1 In-plane compression properties

The compression properties of the CFCSs with three different cell shapes were identified. The corresponding compression behaviors are shown in Fig. 3. The load-displacement curves of three biocomposite corrugated structures displayed similar tendencies, the curves increased linearly to the value of initial peak force (IPF),

followed by a plateau value phase. However, the load-bearing capacity and energy absorption properties showed a significant difference. The CFITCS exhibited the highest compression strength, the trapezoid structure displayed the lowest ones. The stiffness (curve slopes), IPF and energy absorption of the CFITCS were superior to the other two structures (Fig. 3 (a, b)). For instance, the energy absorption of the CFITCS was 1.3 and 2 times that of the other two structures. Therefore, the following studies would focus on the compression behaviors of CFITCS.

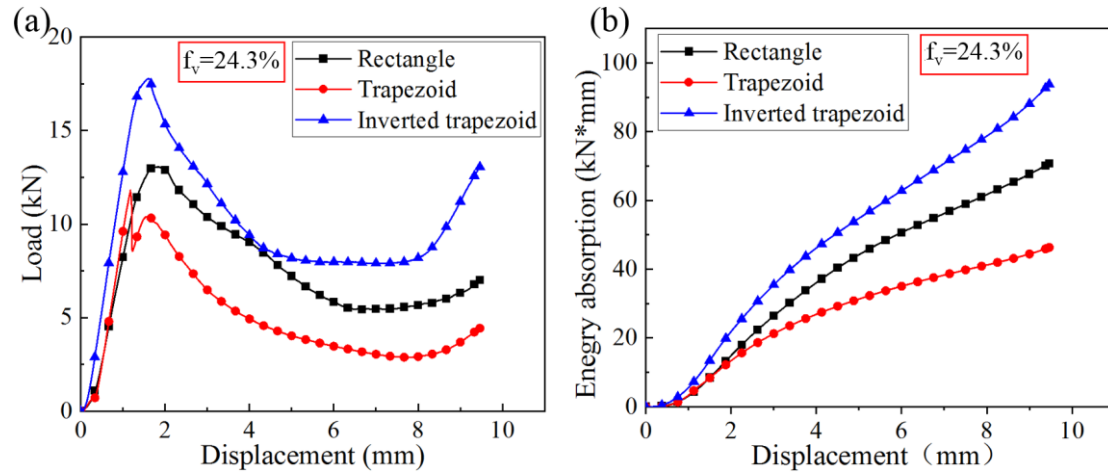


Fig. 3. Effects of cell structures on (a) the compressive properties, and (b) energy absorption capacity of the CFCSs with $f_v = 24.3\%$.

The compression response of CFITCSs with different fiber volume fractions was evaluated. Firstly, the neat matrix structures corresponding to the four fiber volume fractions were tested for comparison. According to a previous study, the addition of ramie fiber improved the mechanical properties of the 3D printed samples [39]. The relationship between f_v and compression behaviors of the CFITCSs is shown in Fig. 4. The evolution of the curves could be divided into three distinct stages

(Fig. 4 (a)). Firstly, the CFITCSs exhibited a linear elastic response up to the maximum load value in the trace. Subsequently, the corrugated-cores yielded and gradually buckled, the cores became more compact, and the load-bearing capacity and stiffness of the samples decreased. Finally, the corrugated-cores were completely compressed, and the samples entered the densification stage.

It can be observed from Fig. 4 (a) that the CFITCSs with different fiber volume fractions exerted an obvious influence on the evolution of the deformation plateau. The CFITCSs with the higher the fiber volume fraction formed deformation plateau of the longer and smoother. In contrast, the stiffness and load-bearing capacity of the CFITCSs decreased with the increase of fiber volume fraction. As shown in Fig. 4 (b), the fiber volume fraction affected IPF. With increasing the fiber volume fraction, IPF of CFITCSs and corresponding fiber-free matrix samples decreased. For instance, compared to samples with $f_v=24.3\%$, the IPF of CFITCS and corresponding fiber-free matrix corrugated structures with $f_v=26.8\%$ decreased by 37.4% and 18.6%, respectively. The CFITCSs generally exhibited larger IPF compared to the corresponding neat matrix samples. However, the IPF of CFITCS with $f_v=26.8\%$ was 17.4% lower than that of the neat matrix sample. Similar trends in EA are observed in Fig. 4 (c). The EA of biocomposite and corresponding matrix corrugated structures decreased as the fiber volume fraction increased. Furthermore, the CFITCSs exhibited larger EA compared to the corresponding neat matrix samples. For example, the EA of CFITCS and corresponding neat matrix sample with $f_v=26.8\%$ decreased by 41.7% and 31.5%, respectively, compared with samples of $f_v=24.3\%$. When $f_v=26.8\%$, the

EA of CFITCS increased by 58.0% compared to the neat matrix sample. As shown in Fig. 4 (d), it can be found that an increase in the fiber volume fraction led to an obvious degradation in the in-plane SEA of the 3D printed CFITCSs. The load-bearing capacity and energy absorption of samples generally decreased as the fiber volume fraction increased (Fig. 4). This was attributable to the significant reduction in the cell wall thickness of the corrugated structures due to the reduction in the amount of matrix. The reduction in wall thickness made the structure easier to yield under compressive loads, resulting in increased structural toughness and reduced strength and stiffness.

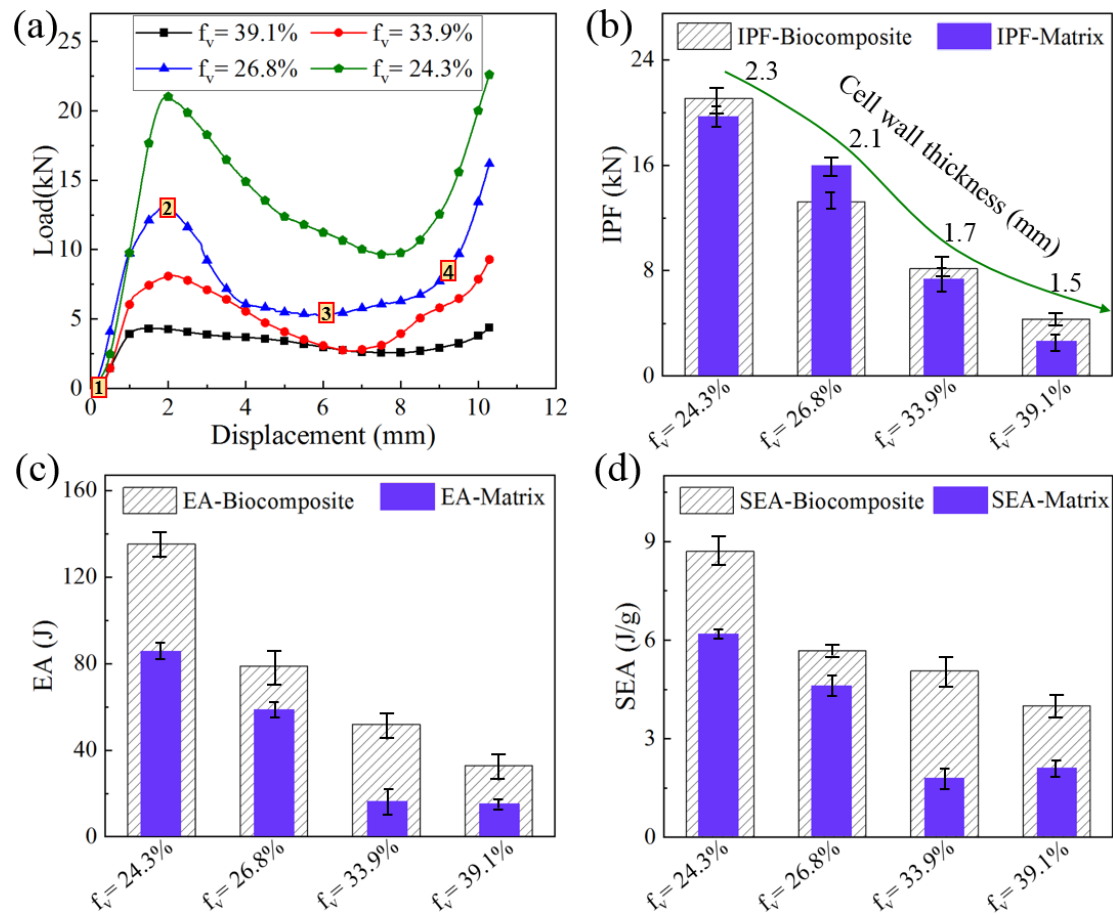


Fig. 4. (a) In-plane compression load-displacement curves, (b) initial peak force (IPF), (c) total energy absorption (EA), and (d) specific energy absorption (SEA) of the

CFITCSs.

3.2 Prediction of the in-plane compression properties

The analytical expression of the in-plane compression strength of a single corrugated web was given and then expanded to evaluate the overall corrugated structures. The predicted strength here referred to the maximum strength of the structure corresponding to IPF. Fig. 5 shows schematic diagrams of a half inverted trapezoid corrugated cell and the inclined web of the cell under in-plane compression. As shown in Fig. 5 (c), l , b and t represent the length of the inclined, the part lateral width and the wall thickness, respectively. Solid and dotted lines denote respectively the initial and deformed web. A virtual displacement δ was applied in the z -direction, along the axial force F_N of the support member as shown in Eq. (3).

$$F_N = \frac{E_s bt}{l} \delta \cos(\theta - 90^\circ) \quad (3)$$

where E_s is the compression modulus of the composite. According to the basic beam theory, the following balance equations could be obtained:

$$\frac{F_s l^2}{2E_s I} - \frac{M_0 l}{E_s I} = 0 \quad (4)$$

$$\frac{F_s l^3}{3E_s I} - \frac{M_0 l^2}{2E_s I} = \delta_s \quad (5)$$

According to Eqs. (4), (5) and Fig. 5 (b), the shear force F_s of the supporting member could be calculated by using Eq. (6).

$$F_s = \frac{12E_s I}{l^3} \delta \sin(\theta - 90^\circ) \quad (6)$$

where $I = bt^3/12$. According to Fig. 5 (b), the total force F in the z-direction can be expressed as follows

$$F = F_N \cos(\theta - 90^\circ) + F_S \sin(\theta - 90^\circ) \quad (7)$$

Combining Eqs. (3) and (6), the total force F was

$$F = \frac{E_S bt}{l} \delta [\cos^2(\theta - 90^\circ) + \frac{t^2}{l^2} \sin^2(\theta - 90^\circ)] \quad (8)$$

The equivalent stress σ_F and strain ε_F applied to the inverted trapezoid corrugated cell can be expressed as:

$$\sigma_F = \frac{F}{b[d - l \sin(\theta - 90^\circ)]} \quad (9)$$

$$\sigma_F = \frac{E_S t \delta}{l[d - l \sin(\theta - 90^\circ)]} [\cos^2(\theta - 90^\circ) + \frac{t^2}{l^2} \sin^2(\theta - 90^\circ)] \quad (10)$$

$$\varepsilon_F = \frac{\delta}{l \cos(\theta - 90^\circ)} \quad (11)$$

Combining Eqs. (10) and (11), the effective compression modulus E_C of the inverted trapezoid corrugated cell could be calculated using Eq. (12).

$$E_C = \frac{t \cos(\theta - 90^\circ) E_S}{d - l \sin(\theta - 90^\circ)} [\cos^2(\theta - 90^\circ) + \frac{t^2}{l^2} \sin^2(\theta - 90^\circ)] \quad (12)$$

The equivalent in-plane compression modulus of CFITCSs with two side panels was:

$$\bar{E} = E_S \frac{2t}{L} + E_C \frac{L - 2t}{L} \quad (13)$$

where L was the length of CFITCSs. During the in-plane compression process, the panels on both sides of CFITCSs fail first. Therefore, the compression strength σ_{pk} of CFITCSs held the following relationship with the compression strength σ_c of the

composite [29]:

$$\frac{\sigma_C}{E_s} = \frac{\sigma_{PK}}{E} \quad (14)$$

The in-plane compression strength of CFITCSs was given as Eq. (15) according to Eqs. (13) and (14).

$$\sigma_{PK} = \left(\frac{2t}{L} + \frac{E_C}{E_s} \frac{L-2t}{L} \right) \sigma_C \quad (15)$$

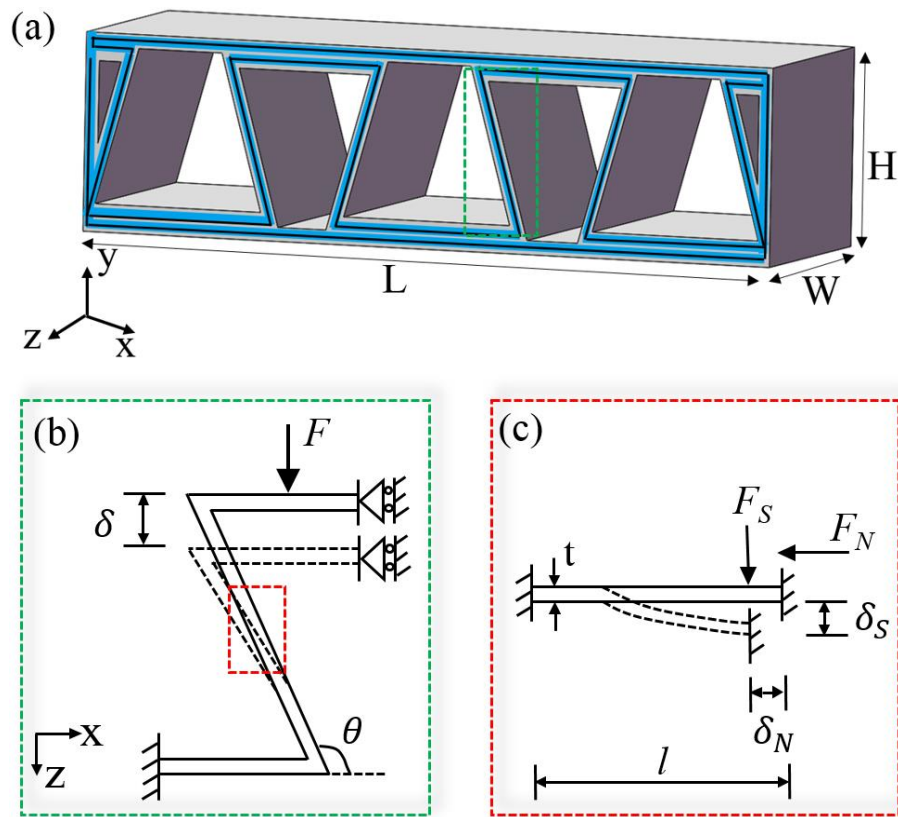


Fig. 5. Schematic diagrams of (a) CFITCSs, (b) a half cell under in-plane compression loading and (c) the inclined web.

The strength predictions of the printed CFITCSs with different f_v under in-plane compression were obtained by Eq. (15). Fig. 6 shows the experimental results of the CFITCSs corresponding to different f_v , and compares them with the analytical

predictions. There was generally a good agreement between experimental measurements and analytical predictions. It could be found that the corrugated structure corresponding to $f_v= 39.1\%$ exhibited the lowest compression strength, which indicates that a too-small wall thickness was undesirable in practical applications. Furthermore, the theoretical strength of CFITCSs was somewhat higher than the measured in-plane strength. This was due to the FFF 3D printing process may cause defects in the corrugated structure.

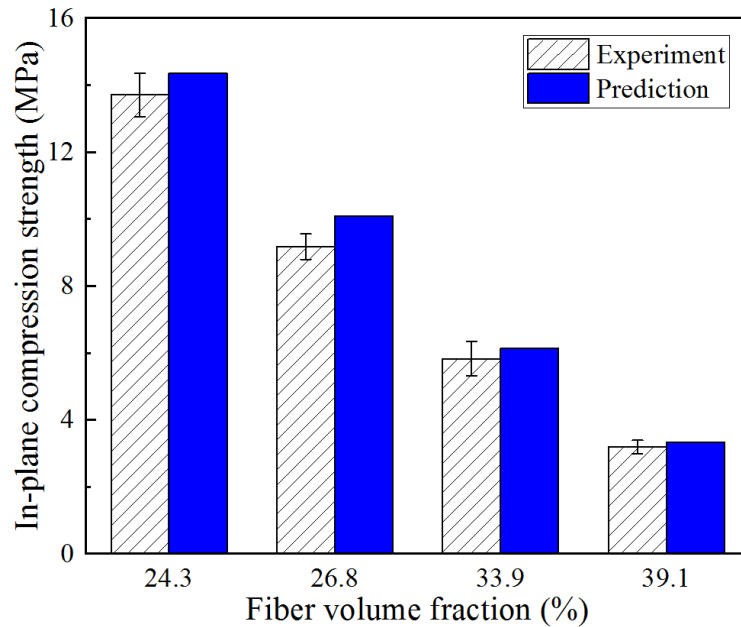


Fig. 6. Comparison of the predicted and experimental results of the CFITCSs under in-plane compressive load.

3.3 Damage process and behavior

The relationship between the progressive damage process of the CFITCSs and the load-displacement curves was established, as shown in Fig. 5 (a) of the yellow square symbols. Upon loading, the sample exhibited a linear elastic response. When the initial peak force was reached (point 2), the CFITCS occurred with the obvious

bending and matrix failure. With further compression, the corrugated-cores buckled and partially collapsed (point 3). Indeed, the curve of Fig. 5 (a) indicates the load-bearing capacity drops rapidly at the onset of instability. Eventually, the CFITCS gradually entered the densification stage (point 4), and the local fracture failure of the corrugated-cores occurred.

Fig. 7 shows the local microscopic morphology of the inverted trapezoid corrugated-cores after in-plane compression testing, it could be observed that the plastic deformation and matrix fracture caused the collapse of CFITCSs. Here, CFITCSs with $f_v= 24.3\%$ and $f_v= 39.1\%$ were used as representatives based on the effect of f_v on damage behavior. As shown in Fig. 7 (a, d), the corrugated-cores underwent a similar deformation and buckling mode under compressive loading. The plastic deformation and matrix fracture generated at the cell nodes caused the collapse of CFITCS. However, the cores exhibited different forms of damage due to the changes in fiber volume fraction. The matrix had severely fractured due to the poor toughness of the CFITCS with $f_v= 24.3\%$ (Fig. 7 (b)). There was a significant difference in the bending resistance of the matrix and the ramie fiber, which caused the severe shearing effect of the fibers, and eventually numerous fibers failed. (Fig. 8 (c)). Comparatively, the fracture surface of the matrix of the corrugated structure with $f_v= 39.1\%$ was not smooth, showing relatively good toughness (Fig. 7 (e)). Under compressive load, the fibers underwent significant bending deformation accompanying plastic deformation of the matrix, and a small number of fibers fractured (Fig. 7 (f)). The CFITCS with higher f_v had lower matrix content and thus

was difficult to fracture.

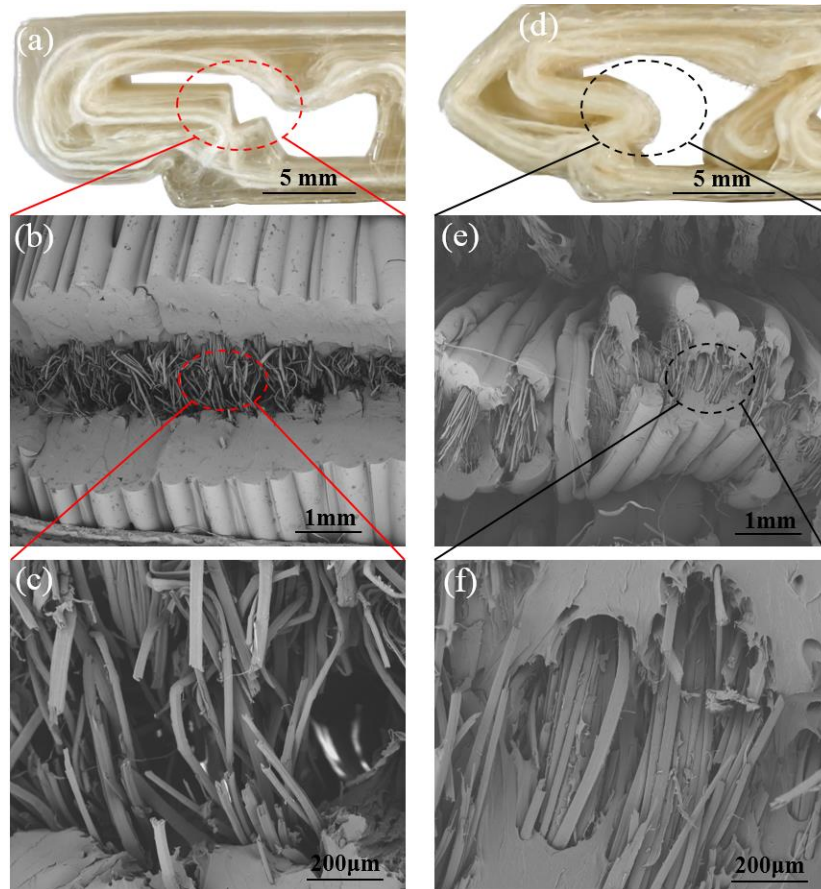


Fig. 7. Damages of the CFITCSs with (a-c) $f_v=24.3\%$, (d-f) $f_v=39.1\%$ after compression tests.

3.4 Shape memory effect

Differential scanning calorimetry (DSC) was performed to characterize the thermal properties of PLA filament and PLA sample. As shown in Fig. 8, it could be found that the glass transition temperature (T_g) of the PLA filament and PLA sample were $57.5\text{ }^\circ\text{C}$ and $64.5\text{ }^\circ\text{C}$, respectively. Therefore, at a water bath temperature of $70\text{ }^\circ\text{C}$ ($T > T_g$) [28], the shape memory PLA matrix in the rubbery state exhibited great deformability and low elastic modulus. As shown in Fig. 9, although the strain during

the compressive process was more than 50%, the corrugated structure did not show any visible fracture. The shape fixed CFCSs after compression were tested for shape memory function. Fig. 9 presents the shape recovery process of the CFITCS with $f_v=39.1\%$, which was completed within 12 s. The shape recovery ratio remained constant for the first 2 seconds because it takes a while to heat the sample completely. Subsequently, the sample started to recover quickly due to the rapid glass transition and strain energy release. It could be found that the maximum shape recovery ratio of the printed CFITCS was about 93.5%, which proved their excellent shape memory performance [21]. Compared to general metal or paper honeycomb structures, the printed CFITCSs showed more potential in applications with shape memory requirements. The integration of natural fibre allowed polymer with high toughness to change and recover shape.

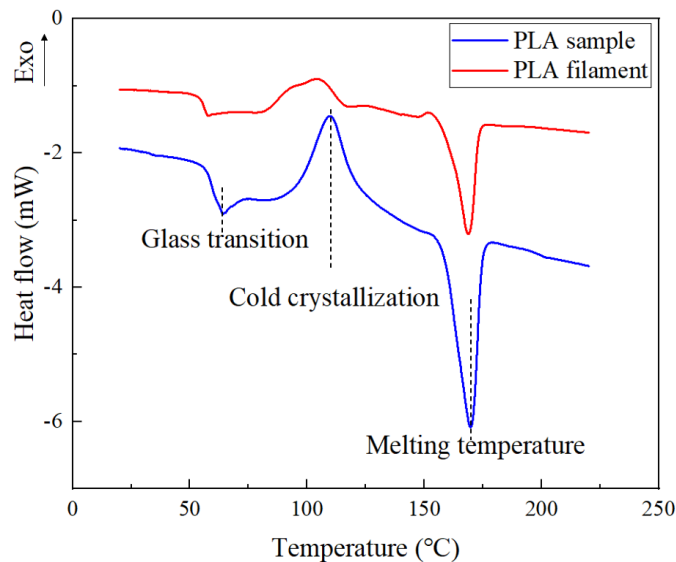


Fig. 8. DSC curves of PLA filament and PLA sample.

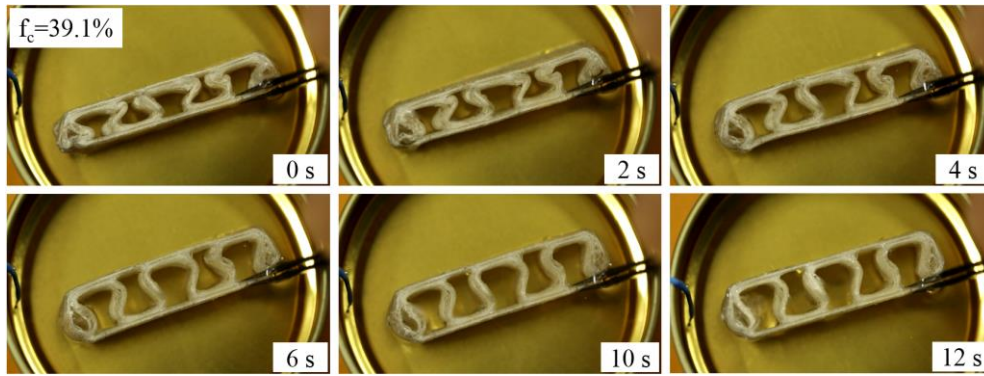


Fig. 9. The shape recovery process of the CFITCS with $f_v=39.1\%$.

The shape memory properties of the CFITCSs with different fiber volume fractions were tested (Fig. 9), and the relationship between the shape recovery ratio and time is shown in Fig. 10. Note that the pure matrix sample fractured after compression due to its poor toughness, and it was impossible to perform the shape recovery test. For all the shape recovery curves, due to the heating process of the samples, the recovery ratio remained unchanged at the beginning, then showed a sharp increase until the maximum recovery ratio was achieved (Fig. 10 (a)). As shown in Fig. 10 (a), it was clear that as the fiber volume fraction increased, the sample recovery time was significantly reduced, and the recovery efficiency was greatly improved. The shape recovery time was reduced from 50 s to 12 s when the fiber volume fraction increased from 24.3% to 39.1% (Fig. 10 (a)). However, the shape recovery ratio was reduced from 95.6% to 93.5%, and the strength was decreased from 20.7 MPa to 4.2 MPa (Fig. 10 (b)). In summary, as the fiber volume fraction increased, the toughness and recovery time of the samples displayed an improvement, whereas the shape recovery ratio and strength decreased.

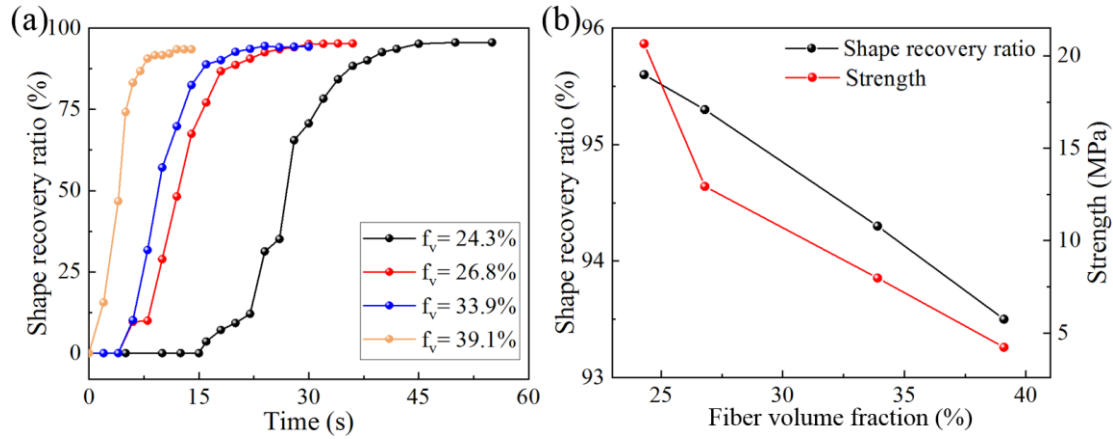


Fig. 10. (a) The shape recovery ratio and (b) the strength of the CFITCSs with different fiber volume fractions.

4. Conclusions

The main goal of this study was to evaluate the effects of cell shapes and fiber volume fractions (f_v) on the compression property of continuous ramie fiber reinforced biocomposite corrugated structures (CFCSs). The CFCSs with three cell shapes were prepared by 3D printing using different designed printing paths. The in-plane compression test was conducted to investigate the mechanical responses. Additionally, continuous natural fiber composite structures for shape memory were proposed for the first time, and the shape memory properties of the CFITCSs were characterized by shape recovery tests.

The compression properties of the CFCSs controlled by reinforced continuous ramie yarn, cell shape and fiber volume fraction (f_v). The addition of continuous ramie fibers significantly improved the compression property of the polylactic acid (PLA) matrix. The CFITCSs presented much higher energy absorption and maximum compression load than those for the other structures. In addition, the compression

properties of CFITCSs were sensitive to the f_v and increased with decreasing f_v (cell thickness increased). The compression process of the CFITCSs could be divided into three distinct stages, including a linear elastic response up to the maximum load value in the trace, the corrugated-cores gradually yielded and buckling stage, and the CFITCSs were completely compressed (densification stage). Besides, the analytical model for the in-plane compression strength of CFITCSs was derived, and predictions showed a good agreement with measurements.

With the increase of fiber volume fraction, the toughness and deformability of the CFITCSs were enhanced. After compression, the sample with an $f_v = 39.1\%$ showed little fiber damage and performed an excellent shape recovery efficiency (12 s). Comparatively, the sample of $f_v = 24.3\%$ had greater stiffness and better load-bearing capacity. The shape recovery time was longer due to severe fracture during compression, but it finally had a better recovery ratio.

Acknowledgements: This work was supported by the National Natural Science Foundation of China (No. 51905555), the Hu-Xiang Youth Talent Program (No. 2018RS3002 and 2020RC3009), the Innovation-Driven Project of Central South University (No. 2019CX017).

Appendix

A: The shape recovery ratio (SRR) was calculated in the following method.

$$SRR = \left(\frac{D'}{D}\right) \div 3 \times 100\% \quad (1)$$

$$\frac{D'}{D} = \left(\frac{L'}{L} + \frac{W'}{W} + \frac{H'}{H}\right) \quad (2)$$

where, D and D' represent the size before compression and the size after recovery. L ,

W and H are the averages of length, width, and thickness of the structures before compression, L' , W' and H' are the averages of length, width, and thickness of the structures after recovery. Here, the averages are the result of three tests.

B: The calculation method of the fiber volume fraction (f_v). According to the extrusion of the materials for FFF 3D printing process, assuming the equal extruded length of matrix filament per unit time, we calculated the fiber volume fraction (f_v) in the following method.

$$V_{\text{fiber}} = \pi \frac{D_f^2 \times L}{4} \quad (1)$$

$$V_{\text{matrix}} = \pi \frac{D_m^2}{4} \times L \times E \quad (2)$$

$$f_v = \frac{V_{\text{fiber}}}{V_{\text{fiber}} + V_{\text{matrix}}} \times 100\% \quad (3)$$

where, V_{fiber} and V_{matrix} represent the volumes of fiber and matrix, and L represents the printing path length. D_f and D_m are the diameters of yarn and matrix filament, E denotes the matrix extrusion. In this work, $L = 100$ mm, $D_f = 0.35$ mm, $D_m = 1.75$ mm.

References

- [1] Wang Z, Li Z, Xiong W. Experimental investigation on bending behavior of honeycomb sandwich panel with ceramic tile face-sheet. *Compos Pt B-Eng.* 2019;164:280-6.
- [2] Carneiro VH, Rawson SD, Puga H, Meireles J, Withers PJ. Additive manufacturing assisted investment casting: A low-cost method to fabricate periodic metallic cellular lattices. *Addit Manuf.* 2020;33:101085.
- [3] Dayyani I, Shaw AD, Saavedra Flores EI, Friswell MI. The mechanics of composite corrugated structures: A review with applications in morphing aircraft. *Compos Struct.* 2015;133:358-80.

- [4] Xu Q, Xiao S, Gao H, Shen H. The propagation of fibre-matrix interface debonding during CFRP edge milling process with the multi-teeth tool: A model analysis. *Compos Pt A-Appl Sci Manuf.* 2022;107050.
- [5] Le Duigou A, Correa D, Ueda M, Matsuzaki R, Castro M. A review of 3D and 4D printing of natural fibre biocomposites. *Mater Des.* 2020;194:108911.
- [6] Xu J, Wu Y, Gao X, Wu H, Nutt S, Yin S. Design of composite lattice materials combined with fabrication approaches. *J Compos Mater.* 2018;53:393-404.
- [7] Zhao X, Wei L, Wen D, Zhu G, Yu Q, Ma ZD. Bending response and energy absorption of sandwich beams with novel auxetic honeycomb core. *Eng Struct.* 2021;247:113204.
- [8] Quadrini F, Squeo E. Injection molding of bushes made of tribological PEEK composites. *Express Polym Lett.* 2007;1:817-23.
- [9] Chacón JM, Caminero MA, Núñez PJ, García-Plaza E, García-Moreno I, Reverte JM. Additive manufacturing of continuous fibre reinforced thermoplastic composites using fused deposition modelling: Effect of process parameters on mechanical properties. *Compos Sci Technol.* 2019;181:107688.
- [10] Fernández-Cervantes I, Morales MA, Agustín-Serrano R, Cardenas-García M, Pérez-Luna PV, Arroyo-Reyes BL et al. Polylactic acid/ sodium alginate/ hydroxyapatite composite scaffolds with trabecular tissue morphology designed by a bone remodeling model using 3D printing. *J Mater Sci.* 2019;54:9478-96.
- [11] Compton BG, Lewis JA. 3D-Printing of Lightweight Cellular Composites. *Adv Mater.* 2014;26:5930-5.
- [12] West AP, Sambu SP, Rosen DW. A process planning method for improving build performance in stereolithography. *Comput-Aided Des.* 2001;33:65-79.
- [13] Kruth JP, Wang X, Laoui T, Froyen L. Lasers and materials in selective laser sintering. *Assem Autom.* 2003;23:357-71.
- [14] Dudek P. FDM 3D Printing Technology in Manufacturing Composite Elements. *Arch Metall Mater.* 2013.
- [15] Wang Q, Tian X, Huang L, Li D, Malakhov AV, Polilov AN. Programmable morphing composites with embedded continuous fibers by 4D printing. *Mater Des.*

2018;155:404-13.

[16] Oladapo BI, Ismail SO, Zahedi M, Khan A, Usman H. 3D printing and morphological characterisation of polymeric composite scaffolds. *Eng Struct.* 2020;216:110752.

[17] Al Abadi H, Thai H-T, Paton-Cole V, Patel VI. Elastic properties of 3D printed fibre-reinforced structures. *Compos Struct.* 2018;193:8-18.

[18] Wang K, Lu Y, Rao Y, Wei N, Ban J, Peng Y et al. New insights into the synergistic influence of voids and interphase characteristics on effective properties of unidirectional composites. *Compos Struct.* 2021;255:112862.

[19] Blok LG, Longana ML, Yu H, Woods BKS. An investigation into 3D printing of fibre reinforced thermoplastic composites. *Addit Manuf.* 2018;22:176-86.

[20] Wang K, Long H, Chen Y, Baniassadi M, Rao Y, Peng Y. Heat-treatment effects on dimensional stability and mechanical properties of 3D printed continuous carbon fiber-reinforced composites. *Compos Pt A-Appl Sci Manuf.* 2021;147:106460.

[21] Dong K, Ke H, Panahi-Sarmad M, Yang T, Huang X, Xiao X. Mechanical properties and shape memory effect of 4D printed cellular structure composite with a novel continuous fiber-reinforced printing path. *Mater Des.* 2021;198:109303.

[22] Melly SK, Liu L, Liu Y, Leng J. On 4D printing as a revolutionary fabrication technique for smart structures. *Smart Mater Struct.* 2020;29:083001.

[23] Yan C, Li G. Design oriented constitutive modeling of amorphous shape memory polymers and Its application to multiple length scale lattice structures. *Smart Mater Struct.* 2019;28:095030.

[24] Hou Z, Tian X, Zhang J, Li D. 3D printed continuous fibre reinforced composite corrugated structure. *Compos Struct.* 2018;184:1005-10.

[25] Sugiyama K, Matsuzaki R, Ueda M, Todoroki A, Hirano Y. 3D printing of composite sandwich structures using continuous carbon fiber and fiber tension. *Compos Pt A-Appl Sci Manuf.* 2018;113:114-21.

[26] Quan C, Han B, Hou Z, Zhang Q, Tian X, Lu TJ. 3d printed continuous fiber reinforced composite auxetic honeycomb structures. *Compos Pt B-Eng.* 2020;187:107858.

- [27] Dong K, Liu L, Huang X, Xiao X. 3D printing of continuous fiber reinforced diamond cellular structural composites and tensile properties. *Compos Struct.* 2020;250:112610.
- [28] Zeng C, Liu L, Bian W, Leng J, Liu Y. Bending performance and failure behavior of 3D printed continuous fiber reinforced composite corrugated sandwich structures with shape memory capability. *Compos Struct.* 2021;262:113626.
- [29] Zeng C, Liu L, Bian W, Leng J, Liu Y. Compression behavior and energy absorption of 3D printed continuous fiber reinforced composite honeycomb structures with shape memory effects. *Addit Manuf.* 2021;38:101842.
- [30] Cheng P, Peng Y, Wang K, Wang Y-Q, Chen C. Study on intralaminar crack propagation mechanisms in single- and multi-layer 2D woven composite laminate. *Mech Adv Mater Struct.* 2021:1-11.
- [31] Goh GD, Yap YL, Agarwala S, Yeong WY. Recent Progress in Additive Manufacturing of Fiber Reinforced Polymer Composite. *Adv Mater Technol.* 2019;4:1800271.
- [32] Yang Y, Fahmy MFM, Pan Z, Zhan Y, Wang R, Wang B et al. Experimental study on basic mechanical properties of new BFRP-bamboo sandwich structure. *Constr Build Mater.* 2020;264:120642.
- [33] Karoyo AH, Dehabadi L, Alabi W, Simonson CJ, Wilson LD. Hydration and Sorption Properties of Raw and Milled Flax Fibers. *ACS Omega.* 2020;5:6113-21.
- [34] Gao S, Liu Y, Wang C, Chu F, Xu F, Zhang D. Structures, Properties and Potential Applications of Corncob Residue Modified by Carboxymethylation. *Polymers.* 2020;12.
- [35] Wang K, Addiego F, Laachachi A, Kaouache B, Bahlouli N, Toniazzo V et al. Dynamic behavior and flame retardancy of HDPE/hemp short fiber composites: Effect of coupling agent and fiber loading. *Compos Struct.* 2014;113:74-82.
- [36] Zhang Y, Qiao J, Zhang G, Li Y, Li L. Prediction of deformation and failure behavior of continuous fiber reinforced composite fabricated by additive manufacturing. *Compos Struct.* 2021;265:113738.
- [37] Zhou N, Yu B, Sun J, Yao L, Qiu Y. Influence of Chemical Treatments on the

Interfacial Properties of Ramie Fiber Reinforced Poly(lactic acid) (PLA) Composites. *J Biobased Mater Bioenergy*. 2012;6:564-8.

[38] Li Q, Li Y, Ma H, Cai S, Huang X. Effect of processing temperature on the static and dynamic mechanical properties and failure mechanisms of flax fiber reinforced composites. *Compos Commun*. 2020;20:100343.

[39] Cheng P, Wang K, Chen X, Wang J, Peng Y, Ahzi S et al. Interfacial and mechanical properties of continuous ramie fiber reinforced biocomposites fabricated by in-situ impregnated 3D printing. *Ind Crops Prod*. 2021;170:113760.